Pseudopulse Near-Field Subsurface Tomography

K. P. Gaikovich,[1] P. K. Gaikovich,[1] Ye. S. Maksimovitch,[2] and V. A. Badeev[2]
[1]*Institute for Physics of Microstructures of RAS, Nizhniy Novgorod, Russia*
[2]*Institute of Applied Physics, National Academy of Sciences of Belarus, Minsk, Belarus*
(Received 22 June 2011; revised manuscript received 15 February 2012; published 19 April 2012)

Decisive success has been achieved in developing the subsurface near-field scanning tomography that overcomes the Rayleigh diffraction limit of a resolution. It is related to the transformation of the multifrequency inverse scattering problem to that for a complex-valued synthesized pulse (pseudopulse). It leads to the integral equation that has maxima in the depth dependence of its kernel and, hence, to the much better depth resolution of tomography. Moreover, the noise related to surface scattering is mainly suppressed in such an approach. This idea is realized here in the microwave subsurface tomography of 3D inhomogeneous dielectric structures. For homogeneous dielectric targets, this approach is applied to obtain holography images of their shape.

DOI: 10.1103/PhysRevLett.108.163902 PACS numbers: 42.30.Wb, 41.20.Jb, 42.25.Fx

The general approach to various methods of computer tomography is based on Radon's transform [1] and the theory of ill-posed problems [2]. The proposed method follows the idea of near-field scanning tomography [3] to its logical end using the possibility of overcoming existing problems by the transformation of the multifrequency inverse scattering problem to that in the time domain. Near-field tomography is based on the property of small-aperture probes to generate or receive evanescent waves, which makes it possible to observe a sounded subsurface object with a subwavelength resolution. This approach is the only way when it is impossible to use higher frequencies (or short pulses)—technically, or, for example, because of the extinction increase. To obtain tomograms, 2D measurements along the interface of the sounded region should be carried out while depending on a third parameter that determines the depth sensitivity (such as signal frequency, probe altitude, or its size). The dependence of the depth sensitivity in the near zone on the probe size and altitude above the interface was first discovered in the thermal radio emission of dielectric media and applied in tomography experiments [3–5].

The statement of 3D inverse scattering problems is typically based on the solution of 3D integral equations of the 1st kind. It leads to limitations of the grid size used at calculations and, hence, to limitations of the achievable resolution. In some of proposed methods (radiometry, impedance, low-frequency sounding of the Earth's crust [3], total-internal-reflection tomography [6,7], multifrequency optics scheme [8] that considers the tip illuminating a sample in free space or the tip illuminated by plane waves together with a sample above the substrate), problems are reduced to one-dimensional integral equations by a 2D inverse Fourier transform over transversal coordinates.

This approach has been developed by us for the scanning tomography of inhomogeneities in arbitrary multilayer media using the proposed method of data acquisition [9]: It involves an analysis of the 2D lateral distribution of the scattered field measured by scanning at the unchanging source-receiver relative position. It enables us to reduce this problem to the solution of the one-dimensional integral equation in the Born approximation. Moreover, an iterative algorithm was proposed to obtain corrections beyond this approximation. Necessary Green functions have been obtained using the plane wave decomposition of fields. The multifrequency and multilevel scheme of measurements have been suggested in this paper, and, to retrieve 3D complex-valued permittivity distributions from the solution of Fredholm integral equations of the 1st kind, algorithms based on the generalized discrepancy principle in the complex Hilbert space W_2^1 have been worked out and studied in the numerical simulation.

This theory has been applied by us to develop the multifrequency microwave tomography of subsurface dielectric inhomogeneities [10]. However, this method, as well as others, proposed in the above-cited papers, remained far from real applications. The main problem consisted of high demands to accuracy of measured data, whereas, in most cases, the scattering by surface inhomogeneities leads to noise level so high that it is difficult to discern the contribution of subsurface targets in the signal. In this Letter, to overcome existing difficulties, we propose the new approach based on the transformation of the multifrequency inverse scattering problem to that for a synthesized pulse.

Theory.—Let us consider a scattering region with the complex permittivity $\varepsilon(\mathbf{r}) = \varepsilon_0 + \varepsilon_1(\mathbf{r})$ that is embedded in a half space $z \leq 0$ with $\varepsilon = \varepsilon_0$ (see Fig. 1). The total field at the frequency ω is a sum of probing and scattered field components $\mathbf{E}(x, y, \omega) = \mathbf{E}_0(x, y, \omega) + \mathbf{E_1}(x, y, \omega)$. For the scheme of measurements with the fixed source-receiver vector $\boldsymbol{\delta}\mathbf{r}$, when the structure of the probing field is invariable relative to the receiver position, it is possible to express the k-space spectrum (2D inverse Fourier transform over x and y) of the scattered field in frameworks of the Born approximation [9]:

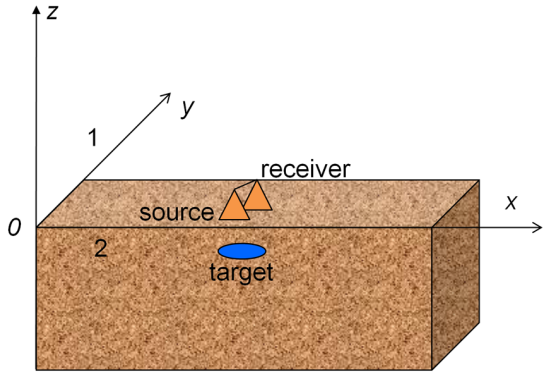

FIG. 1 (color online). Scheme of measurements.

$$E_{1i}(\omega, k_x, k_y, z, \delta\mathbf{r}) = -4\pi^3 i\omega \int_{z'} \varepsilon_1(k_x, k_y, z')\Big\{\int_{-\infty}^{\infty}\int_{-\infty}^{\infty} e^{-i\kappa_x\delta x - i\kappa_y\delta y} \times \int_{z''} [j_i(\omega, \kappa_x, \kappa_y, z'' - z - \delta z) G_{ij}^{12}(\omega, \kappa_x, \kappa_y, z'', z')] \times G_{ji}^{21}(\omega, \kappa_x + k_x, \kappa_y + k_y, z', z) d\kappa_x d\kappa_y dz''\Big\} dz', \quad (1)$$

where G_{ji}^{lk} are k-space components of Green tensors; j_i is the k-space source current distribution (for brevity we use same notations for k-space representations). Variations of complex amplitudes of the received signal s are expressed by the convolution of the instrument function $\mathbf{F}$ of the receiver and the scattered field $\mathbf{E_1}$:

$$s(\mathbf{r}_r) = \int \mathbf{E}_1(\mathbf{r}')\mathbf{F}(x_r - x', y_r - y', z_r, z')dx'dy'dz', \quad (2)$$

where $\mathbf{r}_r$ is the vector determining the receiver position.

From (1) and (2), the transversal spectrum of measured signal variations is obtained as

$$s(k_x, k_y, \omega) = \int_{z'} \varepsilon_1(k_x, k_y, z')K(k_x, k_y, z', \omega)dz'. \quad (3)$$

This equation was used in our algorithm of the microwave subsurface tomography [10] but it was difficult to recognize sounded subsurface objects on the measured image of $s(x, y, \omega)$ against the noise produced by the surface scattering. However, we have found [11] that it is possible to obtain much better images of subsurface targets, using the transformation of multifrequency data to the synthesized pulse

$$s_{\mathrm{re}}(x, y, t) = \mathrm{Re}\int_0^{\infty} s(x, y, \omega)\exp(i\omega t)d\omega \quad (4)$$

that can be represented by its dependence on the effective depth parameter z_s accordingly $s_{\mathrm{re}}(x, y, z_s) = s_{\mathrm{re}}(x, y, t = z_s\,\mathrm{Re}\sqrt{\varepsilon_0}/c)$; the integration is, of course, available over the frequency band $\Delta\omega$ (a similar synthesis has been used in [12] for far-field multifrequency measurements). Subsurface inhomogeneities were clearly seen in near-field images of $s_{\mathrm{re}}(x, y, z_s)$ at some values of z_s that grow with the depth of targets. Also, the strong maximum related to scattering by surface inhomogeneities was seen. It suggests that we make similar transformations in Eq. (3):

$$s(k_x, k_y, t) = \int_0^{\infty} s(k_x, k_y, \omega)\exp(i\omega t)d\omega, \quad (5)$$

where $s(k_x, k_y, z_s) = s(k_x, k_y, t = z_s\,\mathrm{Re}\sqrt{\varepsilon_0}/c)$, which leads to a new equation that relates the complex permittivity spectrum to the complex-valued synthesized pulse of the signal lateral spectrum (we called it pseudopulse for brevity):

$$s(k_x, k_y, z_s) = \int_{z'} \varepsilon_1(k_x, k_y, z')K(k_x, k_y, z', z_s)dz', \quad (6)$$

$K(k_x, k_y, z', z_s) = K(k_x, k_y, z', t = z_s\,\mathrm{Re}\sqrt{\varepsilon_0}/c)$, $K(k_x, k_y, z', t) = \int_0^{\infty} K(k_x, k_y, z', \omega)\exp(i\omega t)d\omega$.

The kernel of the integral in Eq. (6) is formed (after summation over i, j and integration over κ_x, κ_y) by functions that can be expressed as

$$F_{ij}(\kappa_x, \kappa_y, k_x, k_y, z', t) = \int_{\Delta\omega} f_{ij}(\omega, \kappa_x, \kappa_y, k_x, k_y) \times e^{-i(\sqrt{k_0^2\varepsilon_0 - \kappa_x^2 - \kappa_y^2} + \sqrt{k_0^2\varepsilon_0 - (\kappa_x + k_x)^2 - (\kappa_y + k_y)^2})z'}\exp(i\omega t)d\omega, \quad (7)$$

where $k_0 = \omega/c$. The integrand in (7) describes k-space transformations at the scattering. Depending on frequency, the terms of the exponent (the first one related to the sounding field, and the second one related to the scattered field) can correspond to evanescent [if $k_0^2\,\mathrm{Re}\varepsilon_0 < \kappa_x^2 + \kappa_y^2$, $k_0^2\,\mathrm{Re}\varepsilon_0 < (\kappa_x + k_x)^2 + (\kappa_y + k_y)^2$] or to propagating waves. These functions have maxima at some depths $|z'|$ that become deeper with $|z_s|$. Contributions of "evanescent-to evanescent" transformations typically form these maxima near the surface whereas mixed transformations shift maxima deeper. At that, transformations of propagating waves to evanescent components provide a subwavelength resolution to deeper targets than "interevanescent" transformations. "Interpropagating" transformations shift maxima yet deeper. Such a formation leads to the depth dependence of $K(k_x, k_y, z', z_s)$ with maxima that can explain the observed depth selectivity and resolution of pseudopulse images. It can also explain the increase of the near-field response along the z direction that has been observed in [13]. It is well known [5] that kernels with maxima provide better solution results in comparison with the exponential kernel of the initial equation (3).

To solve the Fredholm integral equation (6), the algorithm based on the generalized discrepancy principle in the complex Hilbert space W_2^1 [9] has been applied here to retrieve tomography images of subsurface inhomogeneities with the complex-valued distribution of permittivity. From the solution of (6), the desired 3D structure of

permittivity (tomogram) is obtained by the 2D inverse Fourier transform:

$$\varepsilon_1(x,y,z) = \iint \varepsilon_1(\kappa_x,\kappa_y,z)\exp(i\kappa_x x + i\kappa_y y)d\kappa_x d\kappa_y. \quad (8)$$

In practice, subsurface targets mostly have a homogeneous internal structure. When it is known *a priori* that the permittivity of a target $\varepsilon_1^0 = \text{const}$, the tomography problem can be reduced to the problem of target shape retrieval, i.e., to the problem of computer holography. For that, the k-space permittivity spectrum can be written as a Fourier transform with finite limits:

$$\begin{aligned}\varepsilon_1(k_x,k_y,z) &= \frac{1}{4\pi^2}\int_{y_1}^{y_2}\int_{x_1(y)}^{x_2(y)} \varepsilon_1^0 e^{-ik_x x - ik_y y}dxdy \\ &= \frac{\varepsilon_1^0}{4\pi^2}\int_{y_1}^{y_2}\exp(-ik_y y)\frac{1}{ik_x} \\ &\quad\times (e^{-ik_x x_1(y)} - e^{-ik_x x_2(y)})dy. \quad (9)\end{aligned}$$

Then, making the inverse Fourier transform of (9) over k_y, we obtain the complex-value transcendent equation:

$$\begin{aligned}\varepsilon_1(k_x,y',z) &= \int_{-\infty}^{\infty}\varepsilon_1(k_x,k_y,z)\exp(ik_y y')dk_y \\ &= \frac{\varepsilon_1^0}{2\pi i k_x}(e^{-ik_x x_1(y',z)} - e^{-ik_x x_2(y',z)}), \quad (10)\end{aligned}$$

which is equivalent to the system of two real equations. The desired shape of the target expressed by two functions $x_1(y,z)$, $x_2(y,z)$ is obtained (after change $y' \to y$) from this equation, using the solution $\varepsilon_1(k_x,k_y,z)$ of (6). It should be mentioned that this equation is overdetermined: It can be solved at each value of k_x.

There is a quite simple way to determine the kernel K in (6) from measurements of weakly scattering thin test samples with a known shape and permittivity placed at different depths z_0 throughout the sounded region. Corresponding lateral spectra are expressed as $\varepsilon_1(k_x,k_y,z') = \varepsilon_t(k_x,k_y)\delta(z'-z_0)$. Then the kernel is easily obtained as $K(k_x,k_y,z_0,z_s) = s(k_x,k_y,z_s,z_0)/\varepsilon_t(k_x,k_y)$. If test samples are not weakly scattering, the kernel differs from that in the Born approximation, but it is yet possible to use this calibration for the tomography of objects with a similar level of scattering with a quite good result.

Experiment.—Applying the described approach in experiments with various targets, we have retrieved their tomography images. Measurements of signal complex amplitudes for 801 frequencies in the region of 1.7–7.0 GHz obtained by 2D lateral scanning have been used in the analysis. The source-receiver system based on the vector network analyzer Agilent E5071B includes two identical transmitting and receiving antennas placed in the y direction. They were scanning together in the rectangle x-y area with sizes 30×20 cm above the buried targets.

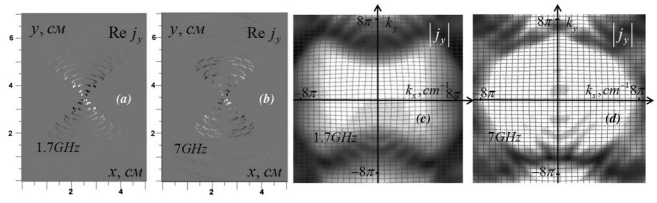

FIG. 2. (a), (b) Current distributions on the bow-tie antenna at 1.7 GHz and 7 GHz. (b), (c) Lateral spectra of these current distributions.

To obtain a subwavelength resolution, the k-space spectrum of the received signal should be broad enough to include evanescent waves. For bow-tie transmitting and receiving antennas (with the length of arms at 3.8 cm and a width of 5.4 cm, placed in the y direction; the fixed distance between the centers of antennas was $\Delta y = 7.5$ cm), used in the measurements, current distributions on the antenna and their spatial spectra are shown in Fig. 2 for the lowest and highest frequencies of the analysis.

As seen in Figs. 2(a) and 2(b), current distributions are quite sharply localized at the center of the antenna's surface, so it has a very broad spatial spectrum [shown in Figs. 2(c) and 2(d)] where components with $k_x, k_y > 2\pi/\lambda$ dominate, and, according to (1), they form a broad near-field spectrum of the signal. It makes it possible to realize the subwavelength resolution of targets in the proposed tomography. Theoretically, the depth of such subwavelength tomography is not limited—restrictions are related only to the achievable sensitivity. It has been demonstrated in our numerical simulation for deeply buried small targets [9]. But, in practice, at a fixed sensitivity, because evanescent components fade with depth, the accuracy of tomography decreases with the target depth whereas its resolution tends gradually toward Rayleigh limitations. Estimations show that, in our case, the sensitivity to inhomogeneities with sizes of about 2 cm remains at depths comparable to the longest wavelength in the analysis (9 cm in the medium). It should also be noted that the accuracy of retrieval depends on depth as well as on

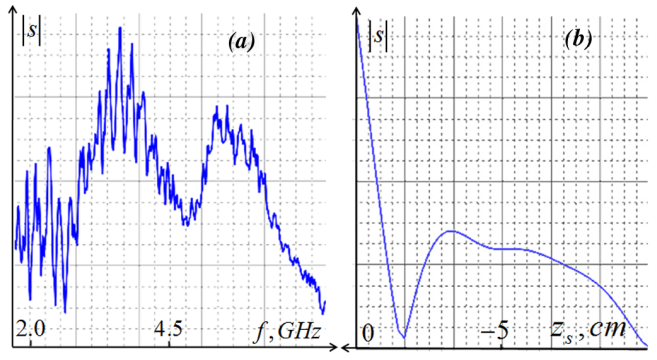

FIG. 3 (color online). (a) Signal spectrum measured above the target ($x = 15$ cm, $y = 10$ cm), $f = \omega/2\pi$. (b) Corresponding pseudopulse amplitude vs effective depth.

the object itself, so it should be obtained in the case study—from numerical or real experiments.

In Fig. 3, the signal spectrum is shown with the corresponding pseudopulse versus the effective depth for a parallelepiped foam sample with sizes $4 \times 3 \times 2$ cm buried in a sandy ground at depth $z = -4$ cm.

As seen in Fig. 3(a), the band of the analysis includes the main part of scattering spectra. The scattering at lower frequencies falls drastically for centimeter-size inhomogeneities; at higher frequencies the signal falls with the increase of absorption. So, it is difficult to achieve a good resolution by a short-pulse sounding at millimeter waves. In Fig. 3(b) one can see the near-surface strong maximum in the pseudopulse amplitude related to the surface scattering at $z_s > -1.5$ cm, and the distribution related to the target scattering at $z_s < -1.5$ cm. It enables us to determine the proper range of analysis at the solution of Eq. (6). In Figs. 4 and 5, 2D images of the measured signal and pseudopulse are shown.

The images demonstrate that the noise related to the surface scattering makes it difficult to discern the sounded sample in images of the measured signal at separated frequencies (Fig. 4), but this noise is much suppressed in images of the pseudopulse (Fig. 5) so that the buried target is clearly seen. It is important to note that the surface of the scanned region was quite smooth, so that such a strong effect of the surface scattering can be explained as the transformation of spatial frequencies at multiple scattering, when small-scale surface inhomogeneities disposed in the strong near field of an antenna produce observed strong large-scale field variations of the signal at each frequency. The discovered possibility of selecting the target scattering from the surface-related noise makes it possible to use stronger signals to detect backscattering from deeper targets.

In Fig. 6, tomography results obtained from the solution of (6) are given. Pseudopulse data at 50 values in the region $-2 \le z_s \le -9$ cm have been used in the analysis to retrieve the target permittivity on the 3D grid with the linear size of 0.25 cm. The corresponding range of the analysis in k-space was $-8\pi \le k_{x,y} \le 8\pi$ cm^{-1} (about the same as in Fig. 2). To demonstrate the role of evanescent waves,

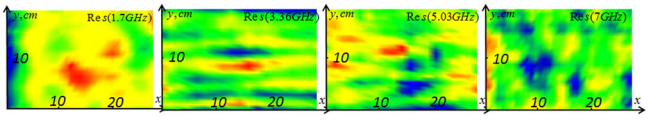

FIG. 4 (color online). Images of measured signal at frequencies 1.7, 3.46, 5.23, and 7 GHz.

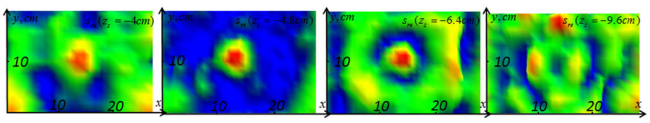

FIG. 5 (color online). Images of pseudopulse at effective depths $z_s = -4.0$, -4.8, -6.4, and -9.6 cm.

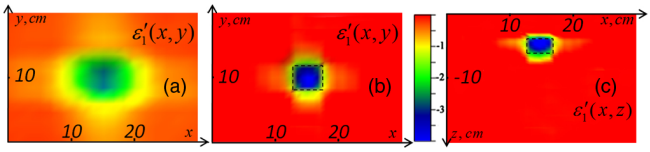

FIG. 6 (color online). Results of subsurface tomography. (a) Horizontal section at depth $z = -5$ cm (retrieval without near-field components). (b) The same as in (a), but retrieved with near-field components. (c) Vertical section at $y = 10$ cm. Dashed lines mark the position and boundaries of the real target.

k-space data with truncated near-field components (at each frequency) have also been used in the analysis. The tomography result with such a truncation is shown in Fig. 6(a) to compare with the retrieval without the truncation in Fig. 6(b) (permittivity images in a horizontal section). The tomography image in a vertical section is shown in Fig. 6(c).

As it is possible to see, the tomography image in Fig. 6(a) looks like a broad blurred spot, whereas the retrieval with near-field components [Figs. 6(b) and 6(c)] is in a good correspondence with parameters of the buried target.

As was mentioned above, it is possible to determine the shape of homogeneous targets using the retrieved k-space permittivity in the solution of (10). Such holography images obtained as functions $x_1(y, z)$, $x_2(y, z)$ for the case shown in Fig. 6 are presented in Fig. 7.

Deviations of retrieved functions from the real shape of the target surface are less than 0.5 cm. Taking into account signal wavelengths in the medium (2.2–9 cm), it demonstrates a subwavelength resolution of the proposed method.

In fact, the developed tomography method is suitable not only for simple homogeneous targets, but also for more complicated distributions of the complex permittivity. To demonstrate these possibilities, a continuous 3D inhomogeneity of complex permittivity produced by the buried sample of melting ice has been studied. For such a strong inhomogeneity, we use the correction of the Born approximation proposed in [9] to take into account the secondary scattering in the iterative algorithm:

$$s^{(n)}(k_x, k_y, z_s) = s(k_x, k_y, z_s) - \Delta s(\varepsilon_1^{(n-1)}, k_x, k_y, z_s) = \int_{z'} \varepsilon_1^{(n)}(k_x, k_y, z') K(k_x, k_y, z', z_s) dz', \quad (11)$$

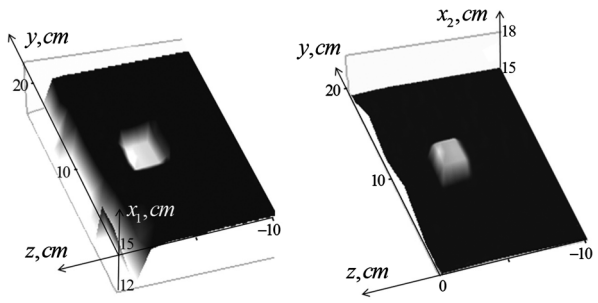

FIG. 7. Holography images of the target shape.

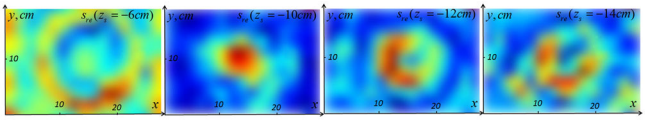

FIG. 8 (color online). Images of synthesized pulse s_{re} at four values of depth parameter $z_s = -6$, -10, -12, and -14 cm.

where $\varepsilon_1^{(0)} = 0$. It is possible to obtain the kernel K in (11) experimentally in the same way, as it was described above, but in this case transfer functions of antennas should be used in the analysis to calculate signal corrections at each step of the solution. In general, it is a very difficult computational task. But it is much simplified for plane antennas, when $s(k_x, k_y, \omega) = \mathbf{F}(k_x, k_y, \omega)\mathbf{E}_1(k_x, k_y, \omega)$. Moreover, for identical transmitting and receiving antennas, it is also possible to use the reciprocity condition $F_i(k_x, k_y, \omega) = \mathrm{const} \times j_i(k_x, k_y, \omega)$.

The studied underground inhomogeneity is formed by the sand-water mixture around the melting ice sample with initial sizes $10 \times 10 \times 4$ cm that has been buried at depth $z = -9$ cm. The scanning has been carried out just in the same way as in the former case, but now the 3D grid with the linear size of 1 cm has been used in the analysis. The corresponding range of these data in k space was $-2\pi \le k_{x,y} \le 2\pi$ cm^{-1}. The permittivity of wet sand is frequency-dependent, so, using De Loor's dielectric mixing formula [14], we have expressed it as $\varepsilon_1(\omega) = \varepsilon_1(4.5\ \mathrm{GHz}) f(\omega)$, including frequency dependence $f(\omega)$ in the kernel part of the equations. At that, it was taken into account that the dielectric parameters for dry sand and ice are very similar.

In Fig. 8 one can see images of the synthesized pulse in the region of measurements at four of 50 values of the effective depth parameter from the region of analysis ($-2 \le z_s \le -20$ cm).

The structure of the studied inhomogeneity formed by melting ice and the region of the wet sand around the ice is clearly seen. In Fig. 9, tomography images obtained from the solution of (11) at the second step of iterations are given for frequency 4.5 GHz.

The results are in a reasonable correspondence with the expected distribution of real and imaginary parts of permittivity related to the buried melting ice. One can see regions of low values both for real and for imaginary parts of permittivity approximately at the position of the ice target. There are also regions of enhanced values of these parameters around the ice location that could be expected because of the enhancement of the water content at the ice melting. It is also seen in Figs. 9(a) and 9(b) that ice sample becomes shorter in the y direction, where, as it is also seen in tomograms, the melting was stronger.

The results show the real feasibility of this method for electromagnetic tomography of absorbing inhomogeneities and open new possibilities in various applications of

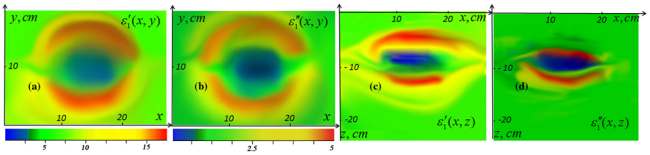

FIG. 9 (color online). Results of tomography of the 3D permittivity underground distribution. Real (a) and imaginary (b) parts of retrieved permittivity $\varepsilon_1(x, y)$ (horizontal sections at depth $z = -9$ cm). Real (c) and imaginary (d) parts of retrieved permittivity $\varepsilon_1(x, z)$ (vertical sections at $y = 10$ cm).

electromagnetic or acoustic physical diagnostics, including biomedical diagnostics of tumors, defectoscopy, civil engineering, antipersonnel mine detection, and underground remote sensing.

This work was supported by the Program of the Russian Academy of Sciences and by the Russian Foundation for Basic Research under Grant No. 12-02-90028-Bel.

[1] J. Radon, *Uber die Bestimmung von Funktionen durch ihre Integralwerte Langs Gewisser Mannigfaltigkiten* (Ber. Verh. Sachs. Akad. Wiss., Leipzig, 1917).
[2] A. N. Tikhonov, V. Y. Arsenin, and A. A. Timonov, *Mathematical Problems of Computer Tomography* (Moscow Press, Nauka, 1987).
[3] K. P. Gaikovich, Phys. Rev. Lett. **98**, 183902 (2007).
[4] K. P. Gaikovich, A. N. Reznik, V. L. Vaks, and N. V. Yurasova, Phys. Rev. Lett. **88**, 104302 (2002).
[5] K. P. Gaikovich, *Inverse Problems in Physical Diagnostics* (Nova Science Publishers Inc., New York, 2004).
[6] P. S. Carney, V. A. Markel, and J. C. Schotland, Phys. Rev. Lett. **86**, 5874 (2001).
[7] P. S. Carney, R. A. Frazin, S. I. Bozhevolnyi, V. S. Volkov, A. Boltasseva, and J. C. Schotland, Phys. Rev. Lett. **92**, 163903 (2004).
[8] B. J. Davis, J. Sunb, J. C. Schotland, and P. S. Carney, J. Mod. Opt. **57**, 809 (2010).
[9] K. P. Gaikovich and P. K. Gaikovich, Inverse Probl. **26**, 125013 (2010).
[10] K. P. Gaikovich, P. K. Gaikovich, Ye. S. Maksimovitch, and V. A. Badeev, in Proceedings of 5th International Conference: Ultrawideband and Ultrashort Impulse Signals, Sevastopol, Ukraine, 2010 (IEEE, Piscataway, NJ, 2010), pp. 156–158, http://ieeexplore.ieee.org/xpl/login.jsp?tp=&arnumber=5609155.
[11] V. A. Mikhnev and V. A. Badeev, in Proceedings of 3rd European Conference on Antennas and Propagation, Berlin, 2009, (IEEE, Piscataway, NJ, 2009), pp. 2234–2235, http://ieeexplore.ieee.org/xpl/login.jsp?tp=&arnumber=5068061.
[12] M. E. Bialkowski, W. Ch. Khor, and S. Crozier, Microw. Opt. Technol. Lett. **48**, 511 (2006).
[13] P. M. Adam, J. L. Bijeon, G. Viardot, and P. Royer, Opt. Commun. **174**, 91 (2000).
[14] J. P. De Loor, J. Microwave Power **3**, 67 (1968).